

DELAD: Deep Landweber-guided deconvolution with Hessian and sparse prior

Tomas Chobola^{1,2}, Anton Theileis³, Jan Taucher³, Tingying Peng^{1,2}

¹Technical University of Munich, Munich, Germany

²Helmholtz AI, Neuherberg, Germany

³GEOMAR Helmholtz Centre for Ocean Research Kiel, Kiel, Germany

Abstract

We present a model for non-blind image deconvolution that incorporates the classic iterative method into a deep learning application. Instead of using large over-parameterised generative networks to create sharp picture representations, we build our network based on the iterative Landweber deconvolution algorithm, which is integrated with trainable convolutional layers to enhance the recovered image structures and details. Additional to the data fidelity term, we also add Hessian and sparse constraints as regularization terms to improve the image reconstruction quality. Our proposed model is *self-supervised* and converges to a solution based purely on the input blurred image and respective blur kernel without the requirement of any pre-training. We evaluate our technique using standard computer vision benchmarking datasets as well as real microscope images obtained by our enhanced depth-of-field (EDOF) underwater microscope, demonstrating the capabilities of our model in a real-world application. The quantitative results demonstrate that our approach is competitive with state-of-the-art non-blind image deblurring methods despite having a fraction of the parameters and not being pre-trained, demonstrating the efficiency and efficacy of embedding a classic deconvolution approach inside a deep network.

Introduction

Image blurring can be mathematically expressed as follows:

$$\mathbf{y} = \mathbf{H}\mathbf{x} + \mathbf{b}, \quad (1)$$

where \mathbf{y} is the blurred image obtained by convolving a sharp image \mathbf{x} with \mathbf{H} , which is a square matrix that approximates the convolution with the PSF, and \mathbf{b} represents the measurement error. Image deconvolution aims to reverse the blurring process and reconstruct the sharp image. Existing image deconvolution methods can be generally divided into **non-blind deconvolution** and **blind deconvolution**, depending on whether \mathbf{H} is known or not.

The recovery of \mathbf{x} from \mathbf{y} is an ill-posed problem (Bertero and Boccacci 1998). In order to obtain an estimation with feasible accuracy, we need to rely on prior information about the image space. The quality of the reconstructed image is typically measured with a cost function as follows,

$$\mathcal{J}(\mathbf{x}) = \mathcal{J}_1(\mathbf{x}) + \lambda \mathcal{J}_2(\mathbf{x}), \quad (2)$$

where $\mathcal{J}_1(\cdot)$ appraises the estimate with respect to the measurements, and $\mathcal{J}_2(\cdot)$ penalises the absence of desired prop-

erties. The parameter λ balances the importance of the second term in relation to the first term.

Related work

Non-blind deconvolution. Early methods for restoring a sharp image given its blurred representation and respective blur kernel include the Wiener filter (Wiener 1949), which imposes a Gaussian assumption on the noise, the Richardson-Lucy algorithm (Richardson 1972), which assumes the noise follows a Poisson distribution, and the Landweber iteration (Landweber 1951). Additionally, multiple methods propose to use an iterative optimization based on MAP estimations (Levin et al. 2007; Krishnan and Fergus 2009), but differ in their employed priors (e.g., global image or local patch-based). Popular priors include total variation (Wang et al. 2008) or hyper-Laplacian priors (Krishnan and Fergus 2009) that help with constraining the solution space and improving the estimation.

Recent deep learning methods use a U-shape network to perform the deconvolution in the image space and to reconstruct the sharp image (Zhang et al. 2017a; Schuler et al. 2013; Zhang et al. 2017b). Particularly, an interesting approach was proposed to integrate the classic Wiener filter into a deep learning application (Dong, Roth, and Schiele 2020). Instead of applying the Wiener filter in standard image space, (Dong, Roth, and Schiele 2020) performs Wiener filtering on deep features extracted by CNNs, which produces less noisy results compared to pure network-based deconvolution algorithms. The Richardson-Lucy algorithm (Richardson 1972) was also combined with deep learning into a model that when pre-trained showed improved deconvolution performance (Li et al. 2022). Recently, Zhao *et al.* (Zhao et al. 2021) took the advantage of a priori knowledge about the sparsity and continuity of biological structures to adapt the Richardson-Lucy method (Richardson 1972) to increase the resolution of live-cell microscopes nearly twofold.

Blind deconvolution. Recovering the clear picture only from its blurred representation without knowing the blur kernel is even more challenging than non-blind deconvolution. Many previous blind deconvolution methods rely on a maximum a posterior (MAP) framework and Bayesian methods (Fergus et al. 2006; Levin et al. 2009; Xu and Jia 2010; Pan

et al. 2016). Usually, the sharp image and the kernel are estimated in an alternating fashion, with further constraints such as L1/L2 norm (Krishnan, Tay, and Fergus 2011) or patch-based prior (Michaeli and Irani 2014) to find the optimal solution. It has also been shown that studying the problem in the frequency domain can lead to high-quality kernel estimation (Pan et al. 2019). The non-blind Richardson-Lucy algorithm (Richardson 1972) has been successfully adapted to estimate the kernel as well, turning it into a blind method (Fish et al. 1995). This observation has been used by Agarwal *et al.* (Agarwal et al. 2020) to replace the initial sharp image and kernel estimates with learnable weights resulting in a deep unfolded Richardson-Lucy framework that outperforms the classic approach.

Our contribution. The contributions of this paper can be summarised as follows: (i) We propose DELAD, a self-supervised approach for non-blind deconvolution embedding the Landweber iteration, a classic method for image deconvolution, into a deep learning model, omitting the need for over-parameterised generative networks which results in a lightweight and effective model. (ii) We integrate the continuity prior as a form of Hessian regularization into the loss function reducing the noise in the resulting sharp image while preserving the underlying image structures. (iii) We apply our proposed DELAD to deconvolve real microscopic plankton images captured by our underwater camera with an extended depth-of-field (EDOF) lens, thereby removing the blurring effects caused by out-of-focus image slices. The source code is publicly available at <https://github.com/ctom2/delad>.

Methodology

We propose a combination of a classic non-blind iterative deconvolution algorithm and deep learning. The objective of the method is to restore a representation of the sharp image based purely on the blurry input image and the appropriate kernel in a *self-supervised* manner. By embedding Landweber iteration (Landweber 1951) into the algorithm we omit the need for using an extensively large neural network to produce the sharp image. We adopt Landweber iteration (Landweber 1951) for its simplicity (Biemond, Lagendijk, and Mersereau 1990) over other iterative deconvolution algorithms such as Richardson-Lucy (Richardson 1972).

Landweber iteration

To obtain the estimate of the sharp image \mathbf{x} from a degraded measurement \mathbf{y} and known kernel \mathbf{H} , following Equation 2, the Landweber algorithm (Landweber 1951; Vonesch and Unser 2008) quantifies the quality of the estimate as

$$\mathcal{J}_1 = \|\mathbf{y} - \mathbf{H}\mathbf{x}\|_2^2. \quad (3)$$

The term measures the residual using the squared L2 norm $\|\cdot\|_2$. By assuming $\lambda = 0$ in Equation 2, the minimiser of the expression becomes the least square estimator given by $\mathbf{x} = \mathbf{H}^\dagger \mathbf{y}$, where

$$\mathbf{H}^\dagger = \lim_{c \rightarrow 0, c > 0} (\mathbf{H}^T \mathbf{H} + c\mathbf{I})^{-1} \mathbf{H}^T \quad (4)$$

is the pseudoinverse of \mathbf{H} . While $\mathbf{H}^\dagger \mathbf{y}$ can be computed in the frequency domain, where \mathbf{H}^\dagger is diagonalised, the method is prone to noisy results as the matrix $\mathbf{H}^T \mathbf{H}$ can have small but non-zero eigenvalues. To prevent the noise amplification, Equation 3 is minimised in an iterative manner by constructing a sequence $(\mathbf{x}^{(n)})_{n \in \mathbb{N}}$ with an initial estimate $\mathbf{x}^{(0)}$ that converges to a minimiser of 3. Applying gradient descent yields the following iterative formula,

$$\mathbf{x}^{(k+1)} = \mathbf{x}^{(k)} + \gamma \mathbf{H}^T (\mathbf{y} - \mathbf{H}\mathbf{x}^{(k)}), \quad (5)$$

where γ denotes the step size.

Deep learning-based Landweber-guided deconvolution with Hessian regularization

To design a deep deconvolution architecture, we propose to embed an explicit Landweber iteration into the model (see Equation 5). We over-parameterize the iterations by substituting the initial estimate $\mathbf{x}^{(0)}$ with a matrix of learnable parameters and by adding correction terms \mathbf{m} , which are also learnable matrices of parameters of the same size as the degraded image \mathbf{y} , to the respective iterations. This Landweber step is projected to non-negative real numbers (denoted as $\mathcal{P}_{\mathbb{R}^+}$) and then passed through a respective convolutional layer \mathcal{C} . We can obtain the deep deconvolution step as follows,

$$\mathbf{x}^{(k+1)} = \mathcal{C}^{(k+1)} \{ \mathcal{P}_{\mathbb{R}^+} [\mathbf{W}] \}, \quad (6)$$

$$\mathbf{W} = \mathbf{x}^{(k)} + \gamma \mathbf{H}^T (\mathbf{y} - \mathbf{H}\mathbf{x}^{(k)}) + \mathbf{m}^{(k+1)} \quad (7)$$

The outputs of the convolutional layers $\mathcal{C}^{(k)}$ are then concatenated and passed to the final layer that unifies the intermediate deconvolution results $\mathbf{x}^{(k)} \forall k > 0$ into a single sharp image estimate $\hat{\mathbf{x}}$.

The terms $\mathbf{x}^{(0)}$, $\mathbf{m}^{(1)}$, $\mathbf{m}^{(2)}$, $\mathbf{m}^{(3)}$ together with the kernels of convolutional layers $\mathcal{C}^{(k)}$ are updated in an iterative *self-supervised* approach as the only information provided to the model is the degraded image \mathbf{y} and the corresponding blur kernel \mathbf{H} . The parameters are optimised to minimise the following loss function,

$$\mathcal{L} = \mathcal{L}_1(\hat{\mathbf{x}} \otimes \mathbf{H}, \mathbf{y}) + \psi \mathcal{R}(\hat{\mathbf{x}}), \quad (8)$$

where $\mathcal{L}_1(\cdot)$ is the negative of the structural similarity index (SSIM) between the degraded image \mathbf{y} and the representation of the sharp image $\hat{\mathbf{x}}$ convolved with the known kernel \mathbf{H} . The loss is moreover regularised with a Hessian prior in the image space

$$\mathcal{R}(X) = \|X_{xx}\|_1 + \|X_{yy}\|_1 + 2\|X_{xy}\|_1, \quad (9)$$

where X_i denotes the second-order partial derivatives of X along the x and y axes. The purpose of the regularisation is to reduce the noise artifacts arising from the deconvolution steps and to preserve the underlying image structure. The strength of the regularisation is controlled by the parameter ψ . Figure 1 illustrates the full model architecture used for obtaining the sharp image estimate $\hat{\mathbf{x}}$ with 3 deep Landweber-guided iterations and the loss function computation.

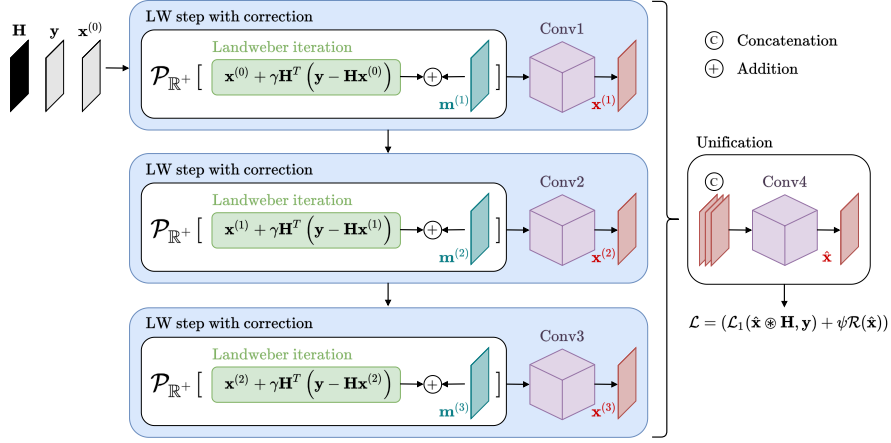


Figure 1: The architecture of the proposed non-blind deconvolution model embedding the Landweber iteration. The terms $x^{(0)}$, $m^{(1)}$, $m^{(2)}$, $m^{(3)}$ together with kernels in the convolutional layers are updated during the optimisation of the model.

Background estimation and sparsity prior for real microscopy image deconvolution

For deconvolution of our EDOF microscopy images we perform pre-processing in a form of background removal (**b** from Equation 1). Moreover, we adapt the loss function by including sparsity as another prior additional to Hessian continuity prior. Sparsity prior has been shown to improve super-resolution microscopy image reconstruction (Zhao et al. 2021).

Background removal. We follow the modified iterative wavelet transform method (Galloway, Le Ru, and Etchegoin 2009) described by Zhao *et al.* (Zhao et al. 2021). We use the residual image arising from setting the values over the mean value of the original image y to zero to estimate the background as follows: (i) The background is iteratively estimated from the lowest frequency wavelet bands related to the input image using 2D Daubechies-6 wavelet filters to decompose the signal up to the 7th level. (ii) An inverse wavelet transform on the lowest band of the frequency information to the spatial domain is performed to prevent the unintended removal of important information. The result is then combined with $\sqrt{y}/2$ into a single image whose pixels consist of the minimum of those two. (iii) The output of the previous step is then used as the input in the next iteration. Following (Zhao et al. 2021), we set the number of iterations to 3 to estimate the background. The final estimated background is then subtracted from the original input image y .

Sparsity. Apart from continuity, another common feature in microscopy imaging is sparsity. We extend the loss function from Equation 8 as follows,

$$\mathcal{L} = \mathcal{L}_1(\hat{x} \circledast H, y) + \psi_1 \mathcal{R}(\hat{x}) + \psi_2 \|\hat{x}'\|_1, \quad (10)$$

where $\|\cdot\|_1$ denotes the L1 norm and \hat{x}' is the color inverted \hat{x} . The reason for the inversion is that our real microscopy images consist of dark objects on light backgrounds, and therefore to enforce sparsity, we need to transform the input image where the background pixel values approach 0.

Experimental results

In this section, we investigate the performance of our proposed method and compare it to other state-of-the-art algorithms. We evaluate DELAD on a wide range of images including traditional computer vision quantitative datasets as well as simulated and real microscopy images.

Implementation and datasets

Implementation details. To balance the computational complexity and efficacy the proposed model embeds three Landweber iterations. The learnable parts of the model are the initial matrix estimate $x^{(0)}$, the correction terms for each iteration $m^{(1)}$, $m^{(2)}$, $m^{(3)}$, and the kernels in the convolutional layers. The matrices are initialised with numbers from a uniform distribution in the interval $[0, 1)$. We set the size of the kernels to be 3×3 for every layer. In each Landweber iteration, we use the step size $\gamma = 0.8$. Next, the projection of the iteration output to non-negative real numbers $\mathcal{P}_{\mathbb{R}^+}(\cdot)$ is done through the ReLU activation function. We use sigmoid as the activation function after each of the convolutional layers.

The optimisation of the model is carried out by the RM-Sprop optimiser for 2000 epochs with the initial learning rate set to 0.05 with a decaying factor of 0.2 when reaching epochs 1000 and 1500. The strength of the continuity prior in the loss function (see Equation 8) is set to $\psi = 1e-6$.

Testing datasets. To benchmark our proposed method and compare it to state-of-the-art methods we use the popular dataset Levin *et al.* (Levin et al. 2009) comprising of four 255×255 grayscale images and 8 motion blur kernels, resulting in a total of 32 blurred images. Further evaluation is done on the Lai *et al.* (Lai et al. 2016) dataset that includes large color images and blur kernels of various sizes. Since the images are split into subsets MANMADE, NATURAL, PEOPLE, SATURATION, and TEXT, we evaluate the methods separately for each set. Moreover, we perform an additional assessment on a dataset of synthetic microscopy images blurred with synthetic kernels following the evaluation

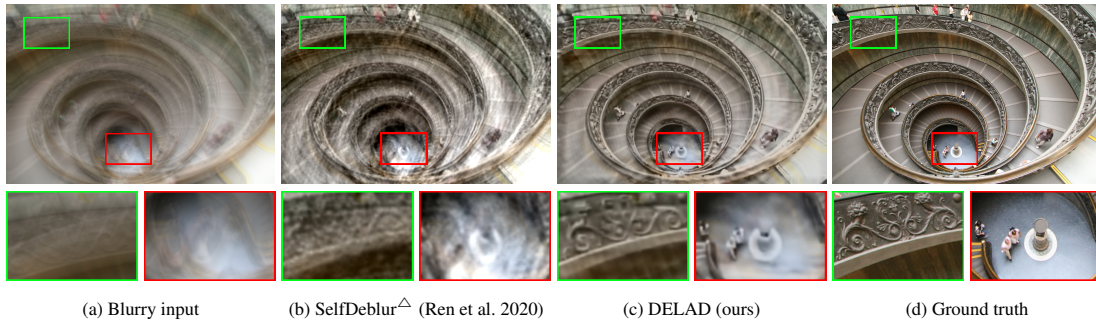


Figure 2: Overview of deconvolution outputs of two self-supervised methods. SelfDeblur $^{\Delta}$ result (Subfigure 2b) was obtained using a blind setting (no prior knowledge of the blur kernel), whereas DELAD result (Subfigure 2c) was obtained using a non-blind setting. The deconvolution with prior knowledge of the blur kernel allows for better reconstruction of the image details.

of the unsupervised deconvolution algorithm proposed by Bredell *et al.* (Bredell et al. 2021). The microscopy dataset takes four sharp synthetic images taken from the simulation of Schneider *et al.* (Schneider et al. 2015) cropped to the size 255×255 . Each sharp image is blurred with one kernel from Levin *et al.* (Levin et al. 2009) and three kernels expected in two-photon microscopy, resulting in a set of 16 blurred images.

Application on real "extended depth-of-field" images.

To prove the functionality of our proposed method in a scientific application, where image blur is a major limiting factor, we evaluate the performance on data obtained by an "extended depth-of-field" (EDOF) plankton imaging system. One major limitation of conventional optical microscopy is the trade-off between magnification and depth-of-field (DOF) which causes the DOF of an optical system to drastically reduce at higher magnifications. Consequently, small objects can only be examined in a very shallow focal plane, which is impractical for many applications that examine an extended sample volume. Image-based observations of plankton require both, a high level of image detail (magnification) and a large image volume (DOF) to collect representative samples of the plankton organisms in water (Lombard et al. 2019). Therefore, we developed a novel underwater imaging system to increase the sample volume while maintaining an optical resolution required to identify plankton ($> 200\mu\text{m}$) by implementing an electrically tunable lens in a telecentric setup. The optical system axially integrates over all focal planes in the entire sample cube during one exposure time. This approach allows to substantially enhance the DOF and image volume while maintaining the desired optical resolution for the identification of plankton. However, as our EDOF image is captured in a single exposure, it contains both in-focus image slices (corresponding to the moving focal plane) and out-of-focus blurry slices (corresponding to those outside the focal range) that reduce the perceived resolution and contrast. Thus, the EDOF-based degradation in image quality makes subsequent data processing and analysis very problematic. So far, no solution exists to remove EDOF blur and improve the optical resolution of such system (see supplementary for the recon-

struction results of EDOF images using SOTA deconvolution methods).

Results on testing images

Results on the dataset of Levin *et al.* (Levin et al. 2009). We evaluate our proposed method on the dataset of Levin *et al.* (Levin et al. 2009) and compare the performance to other state-of-the-art (SOTA) deconvolution algorithms. Besides deep learning based deconvolution methods, we also include a few classic iterative deconvolution methods like Landweber and Richardson-Lucy methods (Landweber 1951; Richardson 1972) in our comparison. Table 2 shows the average PSNR and SSIM values and Figure 4 shows a few exemplary visual comparisons. Firstly, our method significantly outperforms the classic iterative deconvolution algorithms, highlighting the efficiency and efficacy of embedding the iterative formula inside a deep learning application. Secondly, we are able to obtain better results than SelfDeblur (Ren et al. 2020) in blind and non-blind settings, another SOTA self-supervised method, while having less than 11% of the number of parameters of non-blind SelfDeblur (without the kernel generator) (Ren et al. 2020). Lastly, we show in Table 2 the results obtained with our method without the use of the Hessian in the loss function denoted as DELAD $^{-\mathcal{R}}$. While the performance is still high, the SSIM stays behind non-blind SelfDeblur (Ren et al. 2020), showing the necessity of inclusion of the Hessian in the loss function for obtaining better performance.

Results on the dataset of Lai *et al.* (Lai et al. 2016).

While the Levin *et al.* (Levin et al. 2009) dataset consists of grayscale images, the dataset of Lai *et al.* (Lai et al. 2016) contains color images. We used the same approach as Ren *et al.* (Ren et al. 2020) to perform the deconvolution by splitting the images into the YCbCr channels and only doing the optimisation for the Y channel. The average PSNR and SSIM values are shown in Table 1 and the visual comparison is in Figure 3. While SOTA methods that use large pre-trained networks can obtain high-quality reconstructed images, our self-supervised method is still able to obtain very competitive results and even outperform some of the pre-trained networks. Figure 5 highlights the performance

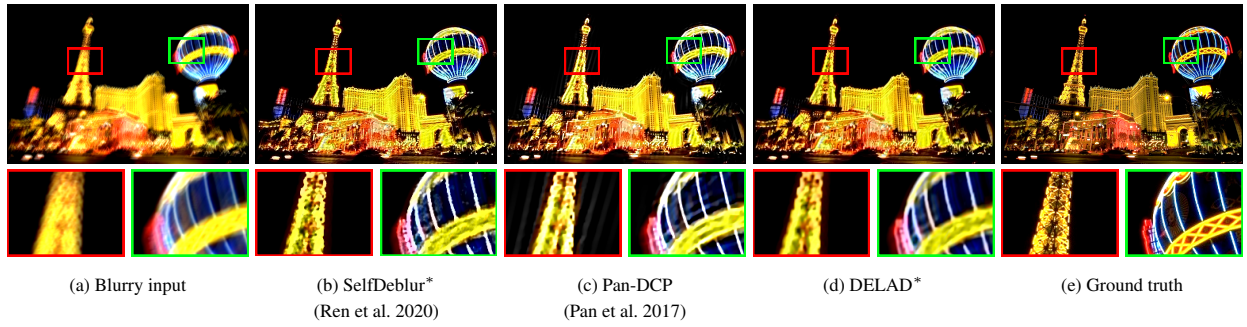


Figure 3: Visual comparison of the deblurring results on the dataset of Lai *et al.* (Lai et al. 2016). Methods marked with * are *self-supervised*.

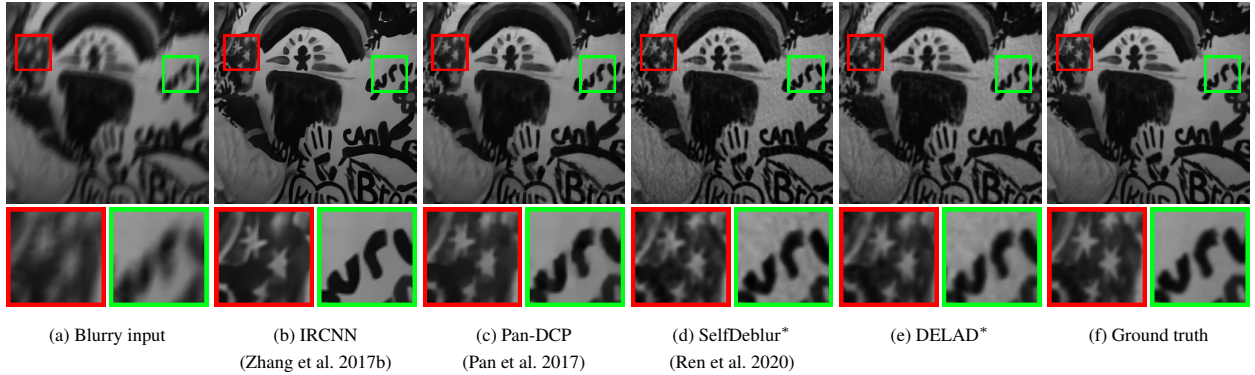


Figure 4: Visual comparison of the deblurring results on the dataset of Levin *et al.* (Levin et al. 2009). Methods marked with * are *self-supervised*.

of the model. From the visual comparison in Figure 3, it can be seen that the inclusion of Hessian prior allows for much smoother structures particularly apparent in the background. Moreover, the continuity assumption in the loss function leads to more polished edges compared to other methods.

Results on microscopy dataset (Bredell et al. 2021). We also evaluate DELAD on simulated microscopy images and show its capacity to deconvolve images similar to a real scenario with a strong blur expected in two-photon microscopy. The quantitative results and comparison with classic iterative algorithms used in deconvolution of microscopy images as well as self-supervised methods are shown in Table 3. Because the simulated images have natural grain in the background, which breaks out the assumption of continuity, we also evaluate our model without the use of the Hessian in the loss function (denoted as $\text{DELAD}^{-\mathcal{R}}$). Indeed, the Hessian regularization naturally suppresses such grain in the deconvolved images, therefore $\text{DELAD}^{-\mathcal{R}}$ achieves better results than DELAD. Both versions of our algorithm outperform other self-supervised deconvolution methods.

Results on real EDOF microscopy images

We then apply our method to real extended-depth-of-field (EDOF) images. We deconvolve all EDOF images with the same kernel simulated following (Liu and Hua 2011) with the Gibson-Lanni model (Gibson and Lanni 1992). Before

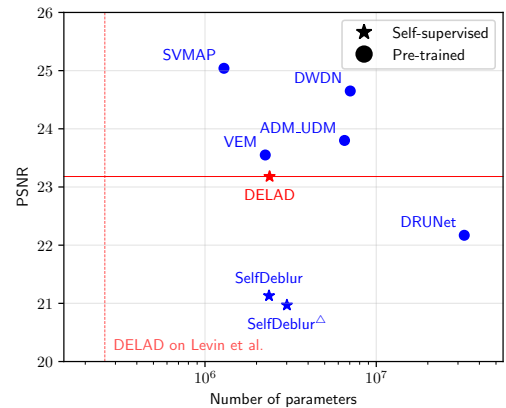


Figure 5: Overview of deconvolution results of state-of-the-art methods (see Table 1) on the dataset of Lai *et al.* (Lai et al. 2016) measured by PSNR (*y*-axis) and their number of parameters (*x*-axis). Notice the *x*-axis being on a logarithmic scale. Δ indicates the deblurring results were obtained using a blind deconvolution setting. We include the number parameters required for deconvolving images from the dataset of Levin *et al.* (Levin et al. 2009) with DELAD as well. Because the terms $\mathbf{x}^{(0)}$, $\mathbf{m}^{(1)}$, $\mathbf{m}^{(2)}$, $\mathbf{m}^{(3)}$ are learnable matrices of the same size as the input image, the number of model parameters changes based on the size of the input.

Table 1: Evaluation of the average PSNR and SSIM of the deblurring results on every class from the dataset of Lai *et al.* (Lai et al. 2016). We highlight the **highest** and the *lowest* values for each class. Note that while our method is completely *self-supervised* it still achieves very competitive results compared to state-of-the-art methods that leverage large pre-trained networks.

Class		Pan-DCP (Pan et al. 2017)	IRCNN (Zhang et al. 2017b)	ADM-UDM (Ko, Chang, and Ding 2020)	DRUNet (Zhang et al. 2021)	VEM (Nan, Quan, and Ji 2020)	DWDN (Dong, Roth, and Schiele 2020)	SVMAP (Dong, Roth, and Schiele 2021)	DELAD
MANMADE	PSNR	<i>18.59</i>	20.47	22.43	20.62	22.71	24.02	23.75	21.94
	SSIM	<i>0.594</i>	0.604	0.724	0.613	0.780	0.836	0.776	0.628
NATURAL	PSNR	<i>22.60</i>	23.26	25.04	23.25	25.29	25.91	26.23	24.84
	SSIM	0.698	0.636	0.733	<i>0.630</i>	0.752	0.814	0.778	0.675
PEOPLE	PSNR	<i>24.03</i>	28.04	28.81	28.04	27.19	30.02	30.88	27.63
	SSIM	0.772	0.843	0.866	0.838	<i>0.723</i>	0.905	0.899	0.830
SATURATED	PSNR	<i>16.52</i>	16.99	17.57	17.14	17.65	17.90	18.75	18.91
	SSIM	0.632	0.642	0.627	0.658	<i>0.600</i>	0.695	0.733	0.666
TEXT	PSNR	<i>17.42</i>	21.37	25.13	21.79	24.92	25.40	25.60	22.56
	SSIM	<i>0.619</i>	0.828	0.883	0.829	0.853	0.877	0.894	0.836
Overall	PSNR	<i>19.89</i>	22.03	23.80	22.17	23.55	24.65	25.04	23.18
	SSIM	<i>0.666</i>	0.710	0.767	0.714	0.742	0.825	0.816	0.727

Table 2: Comparison of the average PSNR and SSIM of the deblurring results on the dataset of Levin *et al.* (Levin et al. 2009) using iteration-based self-supervised deconvolution methods. Δ indicates the deblurring results were obtained using a blind deconvolution setting. DELAD^{- \mathcal{R}} denotes our method without the Hessian in its loss function.

Method	PSNR (dB)	SSIM
LW (Landweber 1951)	18.02	0.568
RL (Richardson 1972)	18.71	0.630
D-URL Δ (Agarwal et al. 2020)	27.12	0.910
IRCNN (Zhang et al. 2017b)	31.89	0.933
Pan-DCP (Pan et al. 2017)	32.69	0.928
SelfDeblur Δ (Ren et al. 2020)	33.07	0.931
SelfDeblur (Ren et al. 2020)	33.32	0.944
DELAD ^{-\mathcal{R}}	34.07	0.938
DELAD	34.35	0.954

Table 3: Comparison of the average PSNR and SSIM of the deblurring results on the microscopy dataset (Bredell et al. 2021) using iteration-based self-supervised deconvolution methods. Δ indicates the deblurring results were obtained using a blind deconvolution setting. DELAD^{- \mathcal{R}} denotes our method without the Hessian in its loss function.

Method	PSNR (dB)	SSIM
LW (Landweber 1951)	9.57	0.166
RL (Richardson 1972)	9.91	0.180
W-DIP Δ (Bredell et al. 2021)	22.12	0.419
SelfDeblur (Ren et al. 2020)	22.44	0.443
DELAD ^{-\mathcal{R}}	23.70	0.640
DELAD	22.88	0.482

the deconvolution step, we estimate and remove the background as described above as a pre-processing step. The background-removed image is then deconvolved using our method that is optimised in 1000 epochs. The initial learning rate is set to $5e-3$ with a decaying factor of 0.2 when reaching epoch 700. During optimisation, Equation 10 is being minimised, where $\psi_1 = 3e-6$ and $\psi_2 = 0.2$. The deconvolution results in Figure 6 show increased contrast and suppression of the haze surrounding the foreground objects, one characteristic blurry pattern in EDOF images. We also plot inverse pixel intensity to show increased contrast and background suppression with our method. Figure 7 further shows the difference in deconvolution performance between DELAD, DELAD^{- \mathcal{R}} (omitting the Hessian from the loss function) and DELAD optimised without the sparsity constraint. Without the Hessian in the loss function, the reconstructed image is noisy and lacks the clarity of the structures and fine details in the image. The inclusion of the Hessian regularization is essential for obtaining smooth recovered objects. Besides Hessian, the sparsity regularization can further elevate the quality of the resulting deconvolved image. The results obtained with DELAD without the sparsity prior in the loss function include noisy patches as the EDOF haze blurry pattern is not completely suppressed, hence demonstrating itself to be an essential part of the algorithm when deconvolving the real EDOF microscopy images. The results shown in Figure 7 highlight the strength of DELAD to increase the contrast, optical resolution, and legibility of the objects on the deconvolved images whereas in the raw EDOF images the animal structures are hardly visible. The improved images thereby facilitate downstream processing (e.g. detection and segmentation) as well as taxonomic classification.

Conclusion

In this paper, we propose a lightweight self-supervised non-blind deconvolution module that embeds a classic iterative deconvolution algorithm into a deep learning application. By integrating convolutional layers into the iterative Landweber deconvolution algorithm we are able to efficiently reconstruct the sharp image. We also explore constraints added to

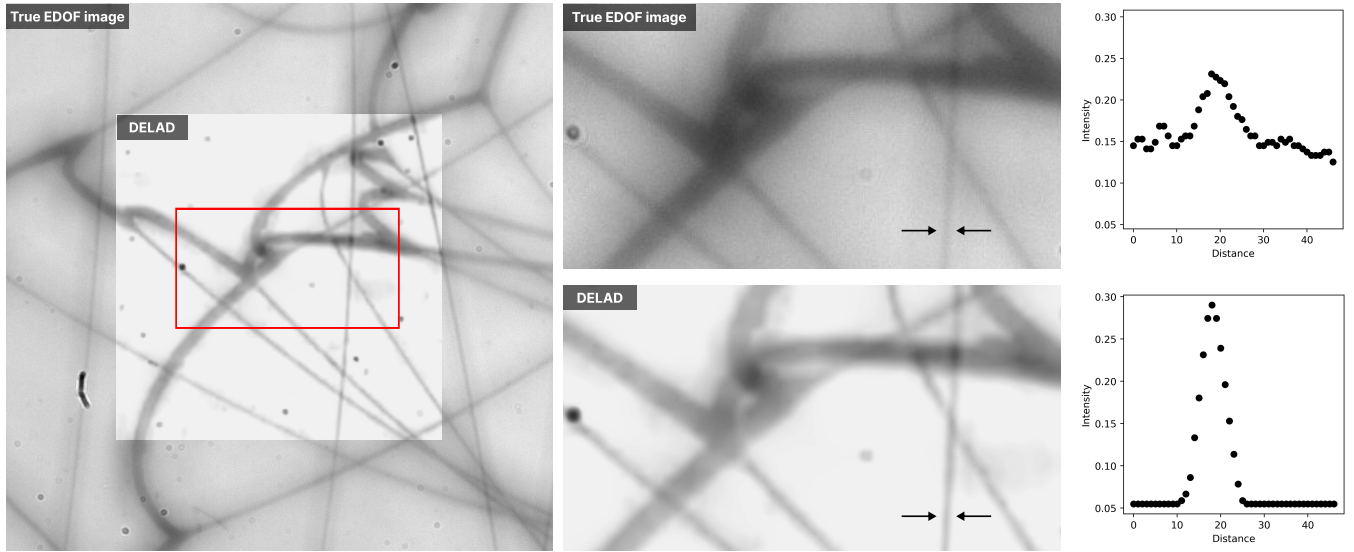


Figure 6: Overview of the sparse deconvolution of real EDOF image obtained by our underwater imaging system. The inverse pixel intensity plots on the right show the background suppression and contrast increase in the deconvolved image compared to the input, which is crucial for subsequent classification and segmentation tasks.

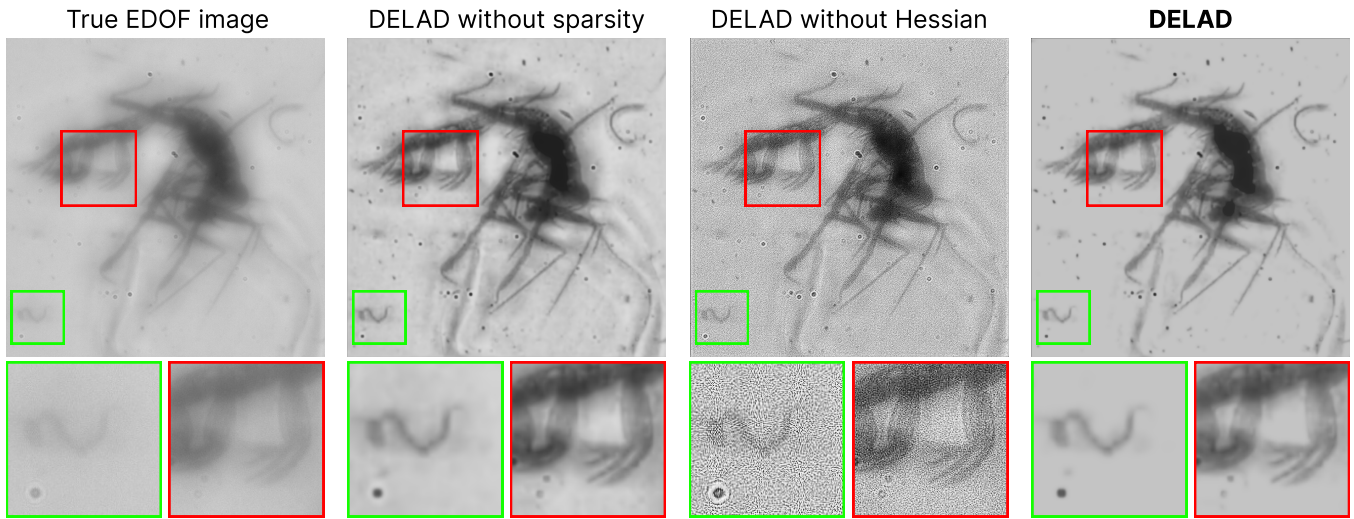


Figure 7: Demonstration of the necessity of Hessian and the sparsity constrain in the loss function. Without the Hessian, the resulting image is noisy with reduced visibility of the fine details and structures in the image. Sparsity smooths the background and improves the overall legibility.

the data fidelity term, Hessian and sparse prior. We show that our model is able to obtain very competitive quantitative results when evaluated on computer vision benchmark datasets, without leveraging any large pre-trained networks and having only a fraction of parameters compared to other SOTA methods. Moreover, we evaluate our method on real microscopy images obtained by our EDOF underwater imaging system showing the capabilities of our model in a real-world application.

References

- Agarwal, C.; Khobahi, S.; Bose, A.; Soltanian, M.; and Schonfeld, D. 2020. DEEP-URL: A Model-Aware Approach to Blind Deconvolution Based on Deep Unfolded Richardson-Lucy Network. 3299–3303.
- Bertero, M.; and Boccacci, P. 1998. *Introduction to Inverse Problems in Imaging*. Institute of Physics Publishing.
- Biemond, J.; Lagendijk, R.; and Mersereau, R. 1990. Iterative methods for image deblurring. *Proceedings of the IEEE*, 78(5): 856–883.
- Bredell, G.; Erdil, E.; Weber, B.; and Konukoglu, E. 2021.

- Wiener Guided DIP for Unsupervised Blind Image Deconvolution. *CoRR*, abs/2112.10271.
- Dong, J.; Roth, S.; and Schiele, B. 2020. Deep Wiener Deconvolution: Wiener Meets Deep Learning for Image Deblurring. In *Proceedings of the 34th International Conference on Neural Information Processing Systems, NIPS'20*. Red Hook, NY, USA: Curran Associates Inc. ISBN 9781713829546.
- Dong, J.; Roth, S.; and Schiele, B. 2021. Learning spatially-variant MAP models for non-blind image deblurring. In *Proceedings of the IEEE/CVF Conference on Computer Vision and Pattern Recognition*, 4886–4895.
- Fergus, R.; Singh, B.; Hertzmann, A.; Roweis, S. T.; and Freeman, W. T. 2006. Removing camera shake from a single photograph. In *ACM SIGGRAPH 2006 Papers*, 787–794.
- Fish, D. A.; Brinicombe, A. M.; Pike, E. R.; and Walker, J. G. 1995. Blind deconvolution by means of the Richardson–Lucy algorithm. *J. Opt. Soc. Am. A*, 12(1): 58–65.
- Galloway, C.; Le Ru, E.; and Etchegoin, P. 2009. An Iterative Algorithm for Background Removal in Spectroscopy by Wavelet Transforms. *Applied spectroscopy*, 63: 1370–6.
- Gibson, S. F.; and Lanni, F. 1992. Experimental test of an analytical model of aberration in an oil-immersion objective lens used in three-dimensional light microscopy. *J. Opt. Soc. Am. A*, 9(1): 154–166.
- Ko, H.-C.; Chang, J.-Y.; and Ding, J.-J. 2020. Deep Priors Inside an Unrolled and Adaptive Deconvolution Model. In *Proceedings of the Asian Conference on Computer Vision*.
- Krishnan, D.; and Fergus, R. 2009. Fast Image Deconvolution Using Hyper-Laplacian Priors. In *Proceedings of the 22nd International Conference on Neural Information Processing Systems, NIPS'09*, 1033–1041. Red Hook, NY, USA: Curran Associates Inc. ISBN 9781615679119.
- Krishnan, D.; Tay, T.; and Fergus, R. 2011. Blind deconvolution using a normalized sparsity measure. In *CVPR 2011*, 233–240. IEEE.
- Lai, W.-S.; Huang, J.-B.; Hu, Z.; Ahuja, N.; and Yang, M.-H. 2016. A Comparative Study for Single Image Blind Deblurring. In *2016 IEEE Conference on Computer Vision and Pattern Recognition (CVPR)*, 1701–1709.
- Landweber, L. 1951. An Iteration Formula for Fredholm Integral Equations of the First Kind. *American Journal of Mathematics*, 73(3): 615–624.
- Levin, A.; Fergus, R.; Durand, F.; and Freeman, W. T. 2007. Image and depth from a conventional camera with a coded aperture. *ACM transactions on graphics (TOG)*, 26(3): 70–es.
- Levin, A.; Weiss, Y.; Durand, F.; and Freeman, W. T. 2009. Understanding and evaluating blind deconvolution algorithms. In *2009 IEEE Conference on Computer Vision and Pattern Recognition*, 1964–1971.
- Li, Y.; Su, Y.; Guo, M.; Han, X.; Liu, J.; Vishwasrao, H. D.; Li, X.; Christensen, R.; Sengupta, T.; Moyle, M. W.; Chen, J.; Usdin, T. B.; Colón-Ramos, D.; Liu, H.; Wu, Y.; and Shroff, H. 2022. Incorporating the image formation process into deep learning improves network performance in deconvolution applications. *bioRxiv*.
- Liu, S.; and Hua, H. 2011. Extended depth-of-field microscopic imaging with a variable focus microscope objective. *Opt. Express*, 19(1): 353–362.
- Lombard, F.; Boss, E.; Waite, A. M.; Vogt, M.; Uitz, J.; Stemmann, L.; Sosik, H. M.; Schulz, J.; Romagnan, J.-B.; Picheral, M.; Pearlman, J.; Ohman, M. D.; Niehoff, B.; Möller, K. O.; Miloslavich, P.; Lara-Lpez, A.; Kudela, R.; Lopes, R. M.; Kiko, R.; Karp-Boss, L.; Jaffe, J. S.; Iversen, M. H.; Irisson, J.-O.; Fennel, K.; Hauss, H.; Guidi, L.; Gorsky, G.; Giering, S. L. C.; Gaube, P.; Gallagher, S.; Dubelaar, G.; Cowen, R. K.; Carlotti, F.; Briseño-Avena, C.; Berline, L.; Benoit-Bird, K.; Bax, N.; Batten, S.; Ayata, S. D.; Artigas, L. F.; and Appeltans, W. 2019. Globally Consistent Quantitative Observations of Planktonic Ecosystems. *Frontiers in Marine Science*, 6.
- Michaeli, T.; and Irani, M. 2014. Blind deblurring using internal patch recurrence. In *European conference on computer vision*, 783–798. Springer.
- Nan, Y.; Quan, Y.; and Ji, H. 2020. Variational-EM-Based Deep Learning for Noise-Blind Image Deblurring. In *Proceedings of the IEEE/CVF Conference on Computer Vision and Pattern Recognition (CVPR)*.
- Pan, J.; Sun, D.; Pfister, H.; and Yang, M.-H. 2016. Blind image deblurring using dark channel prior. In *Proceedings of the IEEE Conference on Computer Vision and Pattern Recognition*, 1628–1636.
- Pan, J.; Sun, D.; Pfister, H.; and Yang, M.-H. 2017. Deblurring images via dark channel prior. *IEEE transactions on pattern analysis and machine intelligence*, 40(10): 2315–2328.
- Pan, L.; Hartley, R.; Liu, M.; and Dai, Y. 2019. Phase-only image based kernel estimation for single image blind deblurring. In *Proceedings of the IEEE/CVF Conference on Computer Vision and Pattern Recognition*, 6034–6043.
- Ren, D.; Zhang, K.; Wang, Q.; Hu, Q.; and Zuo, W. 2020. Neural blind deconvolution using deep priors. In *Proceedings of the IEEE/CVF Conference on Computer Vision and Pattern Recognition*, 3341–3350.
- Richardson, W. H. 1972. Bayesian-Based Iterative Method of Image Restoration*. *J. Opt. Soc. Am.*, 62(1): 55–59.
- Schneider, M.; Hirsch, S.; Weber, B.; Székely, G.; and Menze, B. H. 2015. Joint 3-D vessel segmentation and centerline extraction using oblique Hough forests with steerable filters. *Medical Image Analysis*, 19(1): 220–249.
- Schuler, C. J.; Burger, H. C.; Harmeling, S.; and Schölkopf, B. 2013. A Machine Learning Approach for Non-blind Image Deconvolution. In *2013 IEEE Conference on Computer Vision and Pattern Recognition*, 1067–1074.
- Vonesch, C.; and Unser, M. 2008. A fast thresholded landweber algorithm for wavelet-regularized multidimensional deconvolution. *IEEE transactions on image processing*, 17(4): 539–549.
- Wang, Y.; Yang, J.; Yin, W.; and Zhang, Y. 2008. A New Alternating Minimization Algorithm for Total Variation Image

Reconstruction. *SIAM Journal on Imaging Sciences*, 1(3): 248–272.

Wiener, N. 1949. *Extrapolation, Interpolation, and Smoothing of Stationary Time Series: With Engineering Applications*. The MIT Press. ISBN 9780262257190.

Xu, L.; and Jia, J. 2010. Two-phase kernel estimation for robust motion deblurring. In *European conference on computer vision*, 157–170. Springer.

Zhang, J.; Pan, J.; Lai, W.-S.; Lau, R. W. H.; and Yang, M.-H. 2017a. Learning Fully Convolutional Networks for Iterative Non-Blind Deconvolution. In *Proceedings of the IEEE Conference on Computer Vision and Pattern Recognition (CVPR)*.

Zhang, K.; Li, Y.; Zuo, W.; Zhang, L.; Van Gool, L.; and Timofte, R. 2021. Plug-and-play image restoration with deep denoiser prior. *IEEE Transactions on Pattern Analysis and Machine Intelligence*.

Zhang, K.; Zuo, W.; Gu, S.; and Zhang, L. 2017b. Learning Deep CNN Denoiser Prior for Image Restoration. In *2017 IEEE Conference on Computer Vision and Pattern Recognition (CVPR)*, 2808–2817.

Zhao, W.; Zhao, S.; Li, L.; Huang, X.; Xing, S.; Zhang, Y.; Qiu, G.; Han, Z.; Shang, Y.; Sun, D.-e.; and et al. 2021. Sparse deconvolution improves the resolution of live-cell super-resolution fluorescence microscopy. *Nature Biotechnology*, 40(4): 606–617.